Journal of Materials Chemistry A

Accepted Manuscript

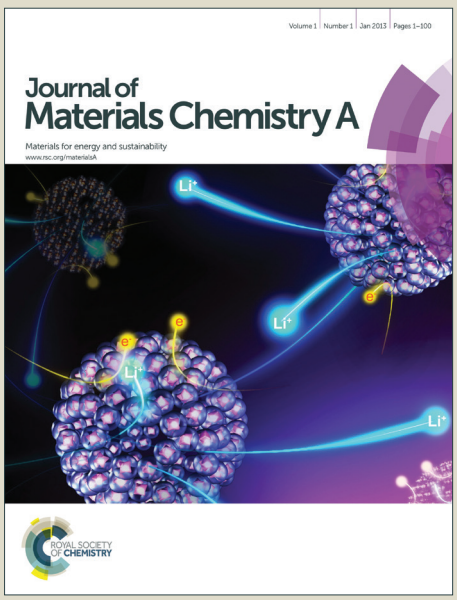

ROYAL SOCIETY OF CHEMISTRY

www.rsc.org/materialsA

Journal Name

RSCPublishing

ARTICLE

Rapid formation of black titania photoanodes: pulsed laser-induced oxygen release and enhanced solar water splitting efficiency

Tomohiko Nakajima,* Takako Nakamura, Kentaro Shinoda and Tetsuo Tsuchiya

Cite this: DOI: 10.1039/x0xx00000x

Received 00th January 2012,
Accepted 00th January 2012

DOI: 10.1039/x0xx00000x

www.rsc.org/

Solar energy is a key part of creating a sustainable society. Pulsed ultraviolet laser irradiation of titania films is a simple process for making oxygen-deficient black titania (TiO_{2-x}) films that use the solar spectrum efficiently. TiO_{2-x} photoanodes were obtained by KrF laser irradiation under low-vacuum conditions for several minutes. The TiO_{2-x} film had a larger absorbance than pristine TiO_2 in the visible light region, and it exhibited a substantial increase in photoelectrochemical water splitting under simulated solar light. The solar-to-hydrogen efficiency of the TiO_{2-x} photoanode reached 0.52%, which was 2.6-fold higher than that of the pristine TiO_2 photoanode. This rapid fabrication process for black titania photoanodes is promising for industrial solar hydrogen production.

Introduction

Photoelectrochemical (PEC) solar water splitting has great potential for providing sustainable energy.[1–5] Photoelectrodes containing semiconductor films for solar water splitting systems have been studied extensively. Improvements in the water splitting efficiency in the visible light region have been reported.[6–9] The *n*-type semiconductor, TiO_2, is the most common photocatalyst because of its high photocatalytic activity, stability, and low cost.[10–12] The wide band gap (~3.2 eV) of TiO_2 reduces the photocatalytic response in the visible light region, which covers the majority of the solar spectrum. However, photocatalytic activity has been increased by improving the visible light response through the use of blackened forms of TiO_2 such as hydrogen-doped TiO_2 (TiO_2:H),[13,14] sulfur-doped TiO_2 (TiO_2:S),[15] and oxygen deficient TiO_{2-x}.[16,17].

However, blackening pristine TiO_2 takes a minimum of several hours because of the low process temperature and hazardous conditions necessary for some methods. For example, TiO_2:H requires annealing at 200 °C for 5 days in high-pressure H_2 gas at 20 bar,[13] TiO_2:S requires annealing at 600 °C for 4 h in H_2S gas,[15] and TiO_{2-x} requires annealing at 500 °C for 6 h under high-vacuum conditions below 0.5 Pa.[16] Therefore, simple, rapid fabrication processes for black titania are desirable.

Recently, ultraviolet (UV) laser-induced crystal nucleation and the growth of oxide thin films from solution have been studied,[18–20] and efficient polycrystalline growth of TiO_2 thin films from a precursor has been reported.[21–23] We have also studied oxygen deficiency induced in a rutile TiO_2 single-crystal surface by pulsed UV laser irradiation.[24] This treatment produced an unconventional metallic state in the oxygen-deficient TiO_{2-x} that was not converted to Ti_nO_{2n-1} Magnéli phases,[25,26] and maintained its original rutile crystal structure with stacking faults. This oxygen deficiency was created by instantaneous photothermal heating under the pulsed UV laser irradiation. Against this background, we aimed to produce polycrystalline black titania photoanodes efficiently by UV laser irradiation of TiO_2 films. We achieved very rapid conversion, within only a few minutes, of a pristine TiO_2 film to an oxygen-deficient TiO_{2-x} film. The blackened film showed a 2.6-fold higher solar-to-hydrogen (STH) efficiency than the pristine film.

Experimental procedure

Sample preparation

The bottom electrode for the photoanode consisted of 10 mol % antimony-doped tin oxide (SnO_2:Sb) films with a thickness of 1.2 μm. (We employed SnO_2:Sb as the bottom electrode in this study since the conducting property of SnO_2:Sb is stable for thermal treatments.) A polycrystalline Al_2O_3 substrate (96%, Kyocera) was spin coated with a dispersion of SnO_2:Sb nanoparticles (99.5%, Alfa Aesar) at 2000 rpm for 5 s. The films were preheated at 400 °C for 10 min and fired at 700 °C for 1 h in air. TiO_2 films were prepared by metal-organic

deposition. The SnO_2:Sb/Al_2O_3 substrates were spin coated with the starting metal-organic solution (0.5 M Ti, SYM-TI05; Symetrix) at 3000 rpm for 10 s. The spin-coated films were preheated at 300 °C for 10 min to convert it to precursor amorphous oxide films by decomposing the organic components. The spin coating and preheating were repeated five times to increase the film thickness to 250 nm. The precursor TiO_2 films were heated at 500 °C for 1 h in air. The TiO_2/SnO_2:Sb/Al_2O_3 specimen was treated as a pristine reference sample. Two post-treatments were carried on the reference TiO_2 films: (1) pulsed KrF laser (Compex110, Lambda Physik) irradiation at a fluence of 50–170 mJ·cm^{-2} for 150 s at 50 Hz with a pulse duration of 26 ns at room temperature under a vacuum of 500 Pa using a rotary pump or in air, and (2) post-annealing at 700 °C for 6 h in air. For optical absorption and electrical resistivity measurements, silica glass substrates were used without the bottom electrode films. We also prepared a titania film by using KrF laser irradiation through the following procedure, called the "irradiation at each deposition" (IED) process. The SnO_2:Sb/Al_2O_3 substrate was spin coated at 3000 rpm for 10 s from the same starting solution as the TiO_2 film. The film was preheated at 300 °C for 10 min and then heated at 500 °C for 10 min in air. The precursor film was irradiated with the KrF laser at 80 mJ·cm^{-2} for 100 s at 50 Hz under a vacuum of 500 Pa at room temperature. This process was repeated five times to increase the film thickness to 250 nm.

Characterization

The phase purity and crystallinity of the TiO_2 thin films on the SnO_2:Sb/Al_2O_3 substrates were determined by grazing incidence X-ray diffraction (GIXRD; SmartLab, Rigaku) with an incidence angle of 0.5°. The surface morphology and cross-sectional structure were determined by scanning electron microscopy (SEM; Hitachi S800). The surface area evaluation was carried out by an atomic force microscope (AFM; Nanopics 2100, SII). The optical absorbance spectra of titania films on silica substrates were recorded with a UV-visible spectrometer (UV-3150, Shimadzu). The electrical resistivity (ρ) of the titania films on silica glass substrates under KrF laser irradiation was measured by using a digital multimeter (KT-2010, Kaise) with two probe contacts. X-ray photoemission spectroscopy (XPS) was carried out using an Al Kα source. Raman spectra were collected by using a laser Raman spectrometer (NRS 7100, Jasco).

Temperature simulations for photothermal heating

Temperature variations during laser irradiation can be described by the heat diffusion equation simplified to describe one-dimensional heat flow[27]

$$\rho C \frac{\partial T}{\partial t} = \kappa \frac{\partial^2 T}{\partial z^2} + \alpha I(z,t)$$

where T is the temperature function at time t and depth z, ρ is the mass density, C is the specific heat capacity, α is the optical absorption coefficient, κ is the thermal conductivity, and $I(z,t)$ is the laser power density. Details of the calculation are explained in the ESI†.

PEC performance evaluation

Under 100 mW·cm^{-2} AM1.5 simulated sunlight (1 SUN) from a 150 W Xe lamp, linear sweep voltammetry for solar water splitting photocurrent measurements was performed in 1.0 M KOH (pH = 13.6) at 0.0–1.5 V vs. a reverse hydrogen electrode (V_{RHE}) in a three-electrode electrochemical cell equipped with a quartz glass window. An Ag/AgCl reference electrode in saturated KCl solution and a Pt wire counter electrode were used, and the scan rate was 5 mV·s^{-1}. The measured potential vs. Ag/AgCl ($V_{Ag/AgCl}$) in the three electrode system was converted to the V_{RHE} according to a following equation: $V_{RHE} = V_{Ag/AgCl} + 0.059pH + V^0_{Ag/AgCl}$, where $V^0_{Ag/AgCl} = 0.1976$ at 25 °C. The STH efficiency (η) of the photoanodes was measured by using the two-electrode configuration cell with the Pt wire as the counter electrode. The following equation was used for estimating STH values: $\eta = J(1.23 - E_{CE})/I_{AM1.5}$, where J is the photocurrent density (mA·cm^{-2}), E_{CE} is the applied bias voltage vs. the counter electrode, and $I_{AM1.5}$ is the irradiance of AM1.5 simulated sunlight at 100 mW·cm^{-2}. Incident photon to current conversion efficiency (IPCE) was evaluated by the three electrode setup with the equation IPCE = $1240J/\lambda I$, where λ is the incident light wavelength (nm), and I is the intensity of the light source at each wavelength (mW·cm^{-2}). The bias voltage was 0.55 V_{RHE}. The monochromatic light was generated using a Xe lamp with optical narrow-band filters. The evolved H_2 gas detection was carried out by using a thermal conductivity detector gas chromatograph (GC-8AIT, Shimadzu).

Results and discussion

Structural and physical properties

Figure 1 shows the surface morphology of the pristine and laser-irradiated samples. As the irradiation fluence increased, a mud-crack pattern associated with volume shrinkage caused by rapid crystallite growth was observed. The in-plane discrete island size was 0.5–1 μm at fluences below 110 mJ·cm^{-2} and 1–2 μm above 140 mJ·cm^{-2}. Above 110 mJ·cm^{-2}, the top TiO_2 surface may have also partially melted, as indicated by the simulated pulsed photothermal heating profiles.

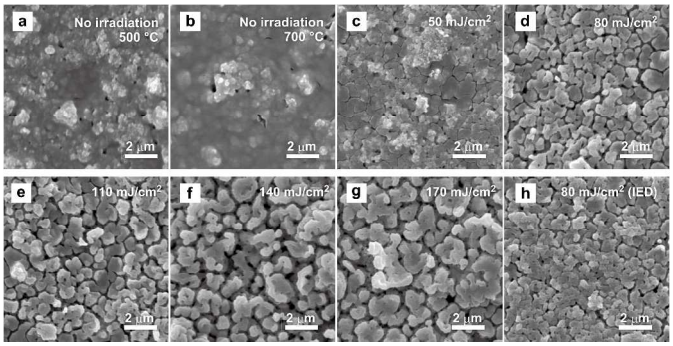

Fig. 1 SEM images of surface morphology for (a) pristine TiO_2/SnO_2:Sb film, (b) TiO_2/SnO_2:Sb film post-annealed at 700 °C, and TiO_{2-x}/SnO_2:Sb films laser

irradiated at (c) 50 mJ·cm^{-2}, (d) 80 mJ·cm^{-2}, (e) 110 mJ·cm^{-2}, (f) 140 mJ·cm^{-2}, (g) 170 mJ·cm^{-2}, and (h) 80 mJ·cm^{-2} (IED).

The crystallinity and structure of the samples were analyzed with the GIXRD patterns (Fig. 2a). The pristine TiO_2 thin film crystallized at 500 °C showed a pure anatase phase. Post-annealing at 700 °C and pulsed UV laser irradiation caused a small amount of phase conversion from anatase to rutile TiO_2. The GIXRD peak intensity of TiO_2 film increased by the laser irradiation in air up to a fluence of 110 mJ·cm^{-2}, and then it decreased above 140 mJ·cm^{-2}. For vacuum irradiation, the diffraction intensity decreased above 50 mJ·cm^{-2} after crystallite growth at 50 mJ·cm^{-2} compared with the pristine sample (Fig. 2b). Larger laser-induced crystallites should grow nearer the surface than the interface, as reported for typical laser-irradiated oxide thin films.[18,20,28] The reduction of the peak intensity indicates that there was no sufficiently coherent periodic structure for stoichiometric TiO_2 near the irradiated surface. The rutile TiO_2 peaks also appeared by the laser irradiation in both air and under vacuum. The quantitative ratio of rutile phase increased with the laser fluence (Fig. 2c).

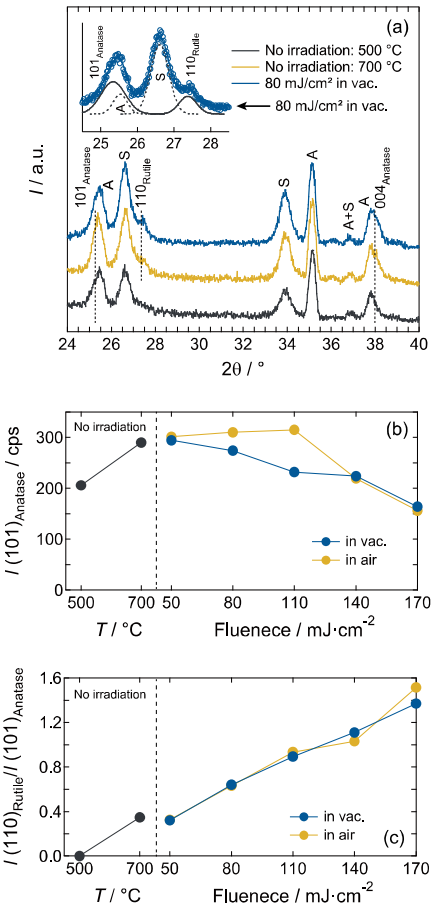

Fig. 2 (a) GIXRD patterns of the pristine TiO_2/SnO_2:Sb film, TiO_2/SnO_2:Sb film post-annealed at 700 °C, and laser-irradiated TiO_{2-x}/SnO_2:Sb films at 80 mJ·cm^{-2}. The subscripts A and S indicate Al_2O_3 and SnO_2:Sb, respectively. (b) Anatase 101 peak intensity of TiO_2 (TiO_{2-x}) films and (c) the peak intensity ratio of TiO_2 rutile 110 and anatase 101 (TiO_{2-x}) films as a function of annealing temperature or laser fluence.

Figure 3 shows photographs of the color of the samples. The pristine TiO_2/SnO_2:Sb film was light gray because of the bottom electrode SnO_2:Sb film. After pulsed laser irradiation in air and under vacuum, the film surface became darker. However, the samples irradiated under vacuum clearly exhibited a homogeneous color, in contrast to the uneven darkening exhibited by the samples irradiated in air. The blackening effect of the laser irradiation was also confirmed by the optical absorbance measurements of the TiO_2 thin films on silica glass for laser irradiation under vacuum at 500 Pa (Fig. 4). The intrinsic optical absorption in the visible range (<400 nm) was clear in the samples irradiated at fluences greater than 80 mJ·cm^{-2}. The increasing optical absorption of visible light also indicates the presence of oxygen deficiency in TiO_2.[16] The light gray color was also confirmed in the sample after the laser irradiation as shown in the inset photographic image in Fig. 4. (The prepared TiO_2 film on the silica substrate looked light pink due to the interference effect because of compact and flat thin film form.)

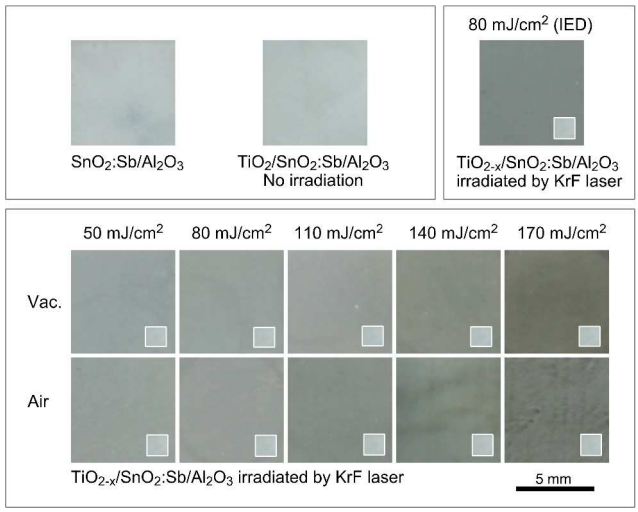

Fig. 3 Photographic images of the SnO_2:Sb/Al_2O_3 and $TiO_2(TiO_{2-x})/SnO_2$:Sb/Al_2O_3 samples with and without pulsed laser irradiation. The insets are the reference color of pristine TiO_2/SnO_2:Sb/Al_2O_3.

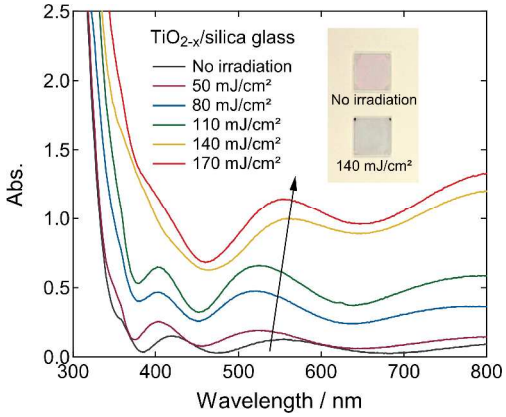

Fig. 4 Optical absorption spectra of $TiO_2(TiO_{2-x})$/silica glass with and without pulsed laser irradiation. The inset photographic image displays the reference pristine TiO_2 film and KrF laser irradiated TiO_{2-x} film at 140 mJ·cm^{-2}.

Figure 5a shows cross-sectional SEM images of the reference sample. A compact TiO_2 film on the bottom SnO_2:Sb electrode is visible. The laser irradiation at 80 mJ·cm^{-2} produced a mud-cracked TiO_{2-x} film with curled edges which also caused the upper part of the SnO_2:Sb bottom electrode to crack. The compact TiO_{2-x} film only covered the top of the bottom electrode, and did not coat the surface in the cracks (Fig. 5b). Therefore, the roughened surface did not increase the surface area of the TiO_{2-x} film. In contrast, the TiO_{2-x} layer covered the entire surface of the mud-cracked bottom electrode in the sample prepared by the IED process at 80 mJ·cm^{-2} (Fig. 5c) through repeated coating and irradiation. In this case, the coated cracks increased the surface area of the TiO_{2-x} film, thus the IED process was expected to enhance the PEC activity. Figure 5d shows the AFM images for these samples. The surface areas of samples for the observed region (4 × 4 μm^2) prepared by conventional and IED laser irradiation were actually calculated to be 123% (20.3 μm^2) and 119% (19.6 μm^2) of reference sample (16.5 μm^2), respective. The surface morphology of each sample is summarized in Fig. 5e

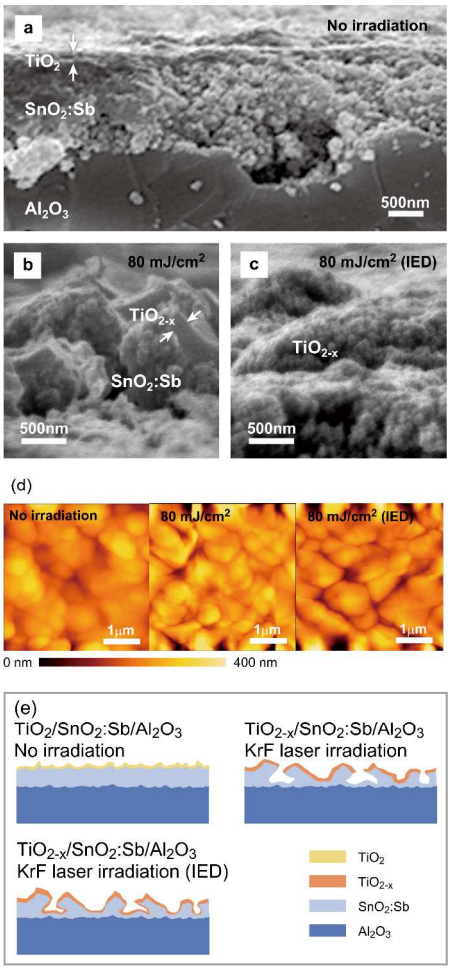

Fig. 5 Cross-sectional SEM images of (a) reference TiO_2/SnO_2:Sb/Al_2O_3 and TiO_{2-x}/SnO_2:Sb/Al_2O_3 prepared by (b) conventional and (c) IED irradiation at 80 mJ·cm^{-2}. (d) AFM images for reference TiO_2/SnO_2:Sb/Al_2O_3 and TiO_{2-x}/SnO_2:Sb/Al_2O_3 prepared by conventional and IED irradiation at 80 mJ·cm^{-2}. (e) Schematic illustrations of the cross-sectional view of the $TiO_2(TiO_{2-x})/SnO_2$:Sb/Al_2O_3 layers.

Figure 6a shows the XPS survey scans of the samples. The peaks for the reference sample were assigned to Ti (2*s*, $2p_{1/2}$ and $2p_{3/2}$) and O (1*s*) from the TiO_2 layer. In the TiO_{2-x} film that was irradiated at 80 mJ·cm^{-2}, additional peaks assigned to Sn ($3d_{3/2}$, $3d_{5/2}$, $3p_{1/2}$ and $3p_{3/2}$) and Sb ($3p_{3/2}$) derived from the bottom electrode were observed because of the surface micro-cracks (Figs. 1d and 5b). However, the Sn and Sb peaks disappeared in the TiO_{2-x} film prepared by IED. The top surface of the cracked SnO_2:Sb bottom electrode in this sample was almost completely covered by TiO_{2-x}. This also suggests that the surface morphology proposed in Fig. 5e is correct.

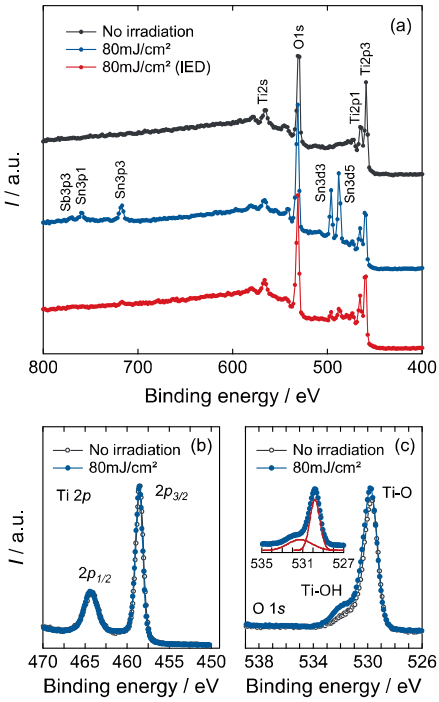

Fig. 6 (a) XPS survey scan for reference TiO_2/SnO_2:Sb/Al_2O_3 and for TiO_{2-x}/SnO_2:Sb/Al_2O_3 prepared by conventional and IED irradiation at 80 mJ·cm^{-2}. (b) Ti 2*p* and (c) O 1*s* spectra for the reference and laser-irradiated (80 mJ·cm^{-2}) samples

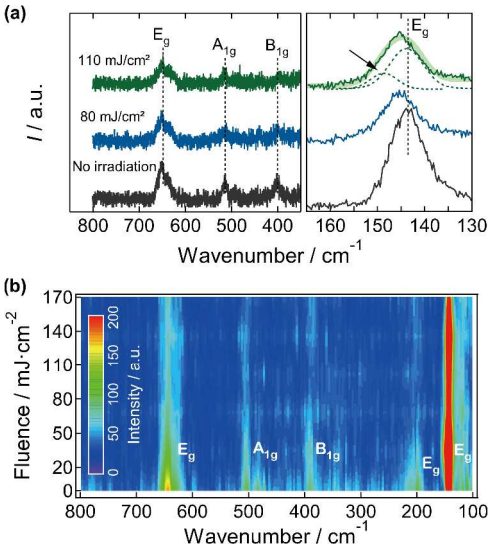

Fig. 7 (a) Raman spectra of pristine TiO_2/silica glass and KrF laser irradiated TiO_{2-x}/silica glass at 80 and 110 mJ·cm^{-2}. (b) Intensity map for irradiated KrF laser fluence and wavelength of Raman spectra

Figure 6b shows the Ti $2p_{1/2}$ and $2p_{3/2}$ XPS peaks of the titania films before and after irradiation at 80 mJ·cm^{-2}. The binding energies of Ti $2p_{1/2}$ and $2p_{3/2}$ were 464.3 and 458.5 eV, respectively, in both samples. These peaks were assigned as Ti^{4+} ions in TiO_2. For the O 1*s* XPS peak, there were two signals assigned to Ti-O bond at 529.8 eV and Ti-OH bond at 531.2 eV.[29] These results suggest that the top surface of oxygen-deficient TiO_{2-x} was reoxidized in the ambient atmosphere after the laser irradiation. The lack of a shift in the Ti and O XPS peaks indicating reoxidization of the top surface has been reported previously for oxygen-deficient black titania.[16,30] A slight increase in the XPS peak corresponding to the Ti-OH bond in the laser-irradiated sample originated from the adsorption of atmospheric humidity at the oxygen-deficient sites, which were created during laser irradiation.

The reoxidation of top surface after the pulsed laser irradiation was confirmed by the XPS studies, nevertheless, the oxygen deficiency in the laser irradiated samples was clearly proved by Raman spectroscopy. Figure 7 shows the irradiated laser fluence dependence of Raman spectra. In the pristine TiO_2 film, the observed peaks were assigned to the E_g modes at 144, 202, and 645 cm^{-1}, the B_{1g} mode at 397 cm^{-1}, and the A_{1g} mode at 515 cm^{-1}. After the pulsed laser irradiation, these peaks were obviously weakened and broadened with the increasing laser fluence. Additionally, a slight blue shift of the peak at 144 cm^{-1} was observed due to an emergence of a new peak at around 150 cm^{-1} (Fig. 7a). This result strongly supports the oxygen deficiency of laser irradiated TiO_2 films as reported in previous works on the oxygen deficient TiO_{2-x}.[16,31,32]

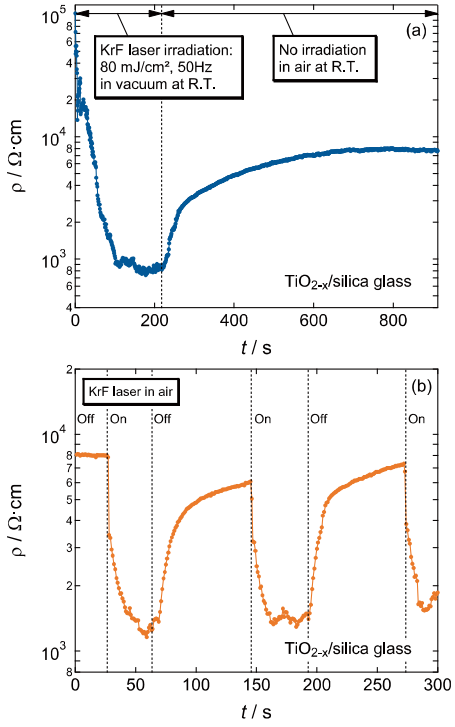

Fig. 8 (a) Electrical resistivity of TiO_2/silica glass under KrF laser irradiation at 80 mJ·cm^{-2} with a repetition of 50 Hz under vacuum. The laser was switched off at 210 s, and air was introduced in the chamber. (b) The KrF laser on/off dependence of ρ for TiO_{2-x}/silica glass.

Figure 8a shows the electrical resistivity (ρ) during laser irradiation. Before irradiation, the pristine TiO_2 film had a very high resistivity of $\rho > 1.5 \times 10^5$ Ω·cm, which was above the measurement limit of the instrument. However, ρ dropped suddenly when laser irradiation at 80 mJ·cm^{-2} under vacuum began, and reached 7.9×10^2 Ω·cm at 180 s after the first laser pulse. This indicates the conductivity was increased by the conduction electrons of Ti^{3+}, which was generated by the oxygen deficiency. After laser irradiation ceased, ρ gradually increased in air, and was saturated at 7.8×10^3 Ω·cm. This result strongly suggests that oxygen was released by the laser irradiation and that the top surface reoxidized after the laser pulse ceased. The laser on/off dependence of ρ for the TiO_{2-x} films is shown in Fig. 8b. ρ cyclically decreased and increased when laser was alternately on and off, respectively. This reversible behavior is also consistent with laser-induced oxygen release and subsequent reoxidation.

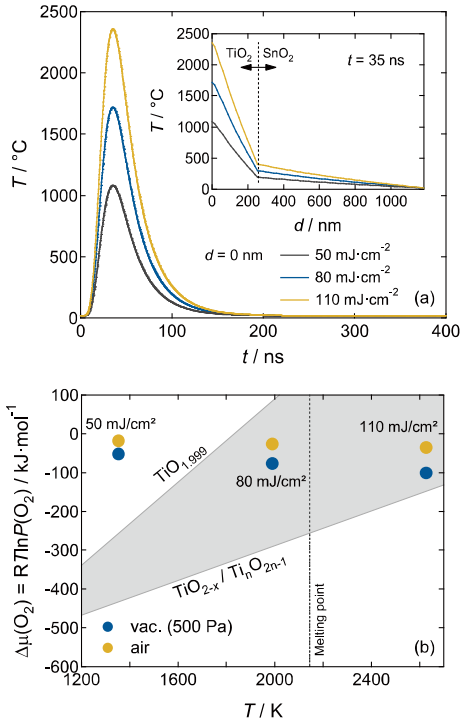

Fig. 9 (a) Simulated temperature variations of TiO_2/SnO_2 under KrF laser irradiation at 50, 80 and 110 mJ·cm^{-2} as a function of time at the film surface, and as a function of depth 35 ns after the incident laser pulse (inset). (b) Ellingham diagram for TiO_2/TiO_{2-x}, and the positions of the samples processed at 50, 80, and 110 mJ·cm^{-2} under vacuum at 500 Pa and in air are plotted from the simulated maximum temperature.

Next, we discuss the laser irradiation process for the TiO_2 films using the temperature simulations shown in Figs. 9a and S1. The calculation for the bottom SnO_2:Sb electrode was approximated by undoped SnO_2. The irradiated KrF laser pulse causes instantaneous heating, and the calculated temperature

reaches a maximum of 1081, 1718, and 2354 °C at 35 ns after the incident pulse at fluences of 50, 80, and 110 mJ·cm^{-2}, respectively. Thereafter, the temperature is quenched to 20 °C. The depth profile reveals that elevated temperature was highest at the film surface and it drops toward the substrate interface. In the Ellingham diagram,[33] the calculated maximum temperature at 80–110 mJ·cm^{-2} at the TiO_2 film surface in air and under vacuum at 500 Pa was in the ideal region for oxygen-deficient TiO_{2-x}, whereas TiO_2 appeared to be still stable at 50 mJ·cm^{-2} (Fig. 9b). The photothermal heating and rapid quenching achieved by pulsed laser irradiation successfully captured the high-temperature phase. The oxygen-deficient content (x) may have had a gradient profile because of the temperature gradient from the surface (Fig. 9a) if sufficient oxygen diffusion did not occur after the laser pulse ceased (quenching temperature). Irradiation at 110 mJ·cm^{-2} would be suitable for creating oxygen deficiencies in the TiO_2 film; however, it reaches temperatures above the melting point of TiO_2 (1843 °C).[34] This produced the large cracks observed in the samples irradiated at 140 and 170 mJ·cm^{-2}. Thus, on the basis of the optical absorption, electrical resistivity, and temperature simulations under laser irradiation, we conclude that the pulsed UV laser irradiation successfully induced oxygen deficiencies in TiO_2 films, and this process was effective to form rapidly black titania photoanodes.

PEC property for solar water splitting

Linear-sweep photovoltammetry was carried out to evaluate the PEC property of pristine TiO_2 and oxygen-deficient TiO_{2-x} photoanodes for solar water splitting (Fig. 10a). The photocurrent density of the pristine TiO_2 film at 1.23 V_{RHE} was 0.503 mA·cm^{-2}, and the onset potential was 0.200 V_{RHE}. The maximum η was 0.20% at 0.645 V_{CE} (Fig. 10b). In the TiO_{2-x} films prepared by laser irradiation under vacuum, the photocurrent density at 1.23 V_{RHE} increased substantially with the irradiated laser fluence up to 110 mJ·cm^{-2}, and then decreased above 140 mJ·cm^{-2}. Moreover, the onset potential (E_{onset}) was lower in samples that were irradiated at laser fluences of 50–110 mJ·cm^{-2} compared with the pristine TiO_2 photoanode.

Table 1 Photoelectrochemical properties of TiO_2 and TiO_{2-x} photoanodes

Preparation condition[a]	$J_{1.23V}$[b] / mA·cm^{-2}	J_{OP}[c] / mA·cm^{-2}	E_{OP} / V_{CE}	η_{max} / %	E_{onset} / V_{RHE}
HT: 500 °C	0.503	0.310	0.645	0.20	0.200
HT: 700 °C	0.381	0.290	0.575	0.19	0.100
LV: 50 mJ·cm^{-2}	0.779	0.585	0.590	0.36	0.135
LV: 80 mJ·cm^{-2}	0.863	0.667	0.560	0.45	0.145
LV: 110 mJ·cm^{-2}	0.908	0.660	0.600	0.39	0.185
LV: 140 mJ·cm^{-2}	0.685	0.443	0.620	0.26	0.290
LV: 170 mJ·cm^{-2}	0.491	0.307	0.640	0.18	0.340
LV2: 80 mJ·cm^{-2}	1.029	0.768	0.560	0.52	0.175
LA: 50 mJ·cm^{-2}	0.761	0.523	0.585	0.34	0.190
LA: 80 mJ·cm^{-2}	0.786	0.590	0.575	0.38	0.115
LA: 110 mJ·cm^{-2}	0.670	0.455	0.605	0.28	0.225
LA: 140 mJ·cm^{-2}	0.578	0.396	0.610	0.23	0.235
LA: 170 mJ·cm^{-2}	0.509	0.308	0.620	0.18	0.300

[a]HT, heat treatment; LV, laser treatment under vacuum; LV2, laser treatment under vacuum using the IED process; and LA, laser treatment in air. [b]Current density at 1.23 V_{RHE}. [c]Current density at E_{OP} V_{CE}.

The sample irradiated at 80 mJ·cm^{-2} showed the highest maximum η (η_{max}) of 0.45%, because the optimum potential for η_{max} (E_{OP}) reached a minimum (0.560 V_{CE}) at this laser fluence (Table 1 and Fig. 10c). High laser fluences greater than 110 mJ·cm^{-2} that resulted in excessive photothermal heating should negatively influence extrinsic transport in TiO_{2-x}/SnO_2:Sb. The variation of E_{OP} and η_{max} as a function of the laser fluence for irradiation in air was the same as that under vacuum (Figs. 10c and S2). However, the vacuum process produced a higher η_{max} and reduced the effective bias voltage. This is probably because of the homogeneous oxygen release at the film surface (Fig. 3).

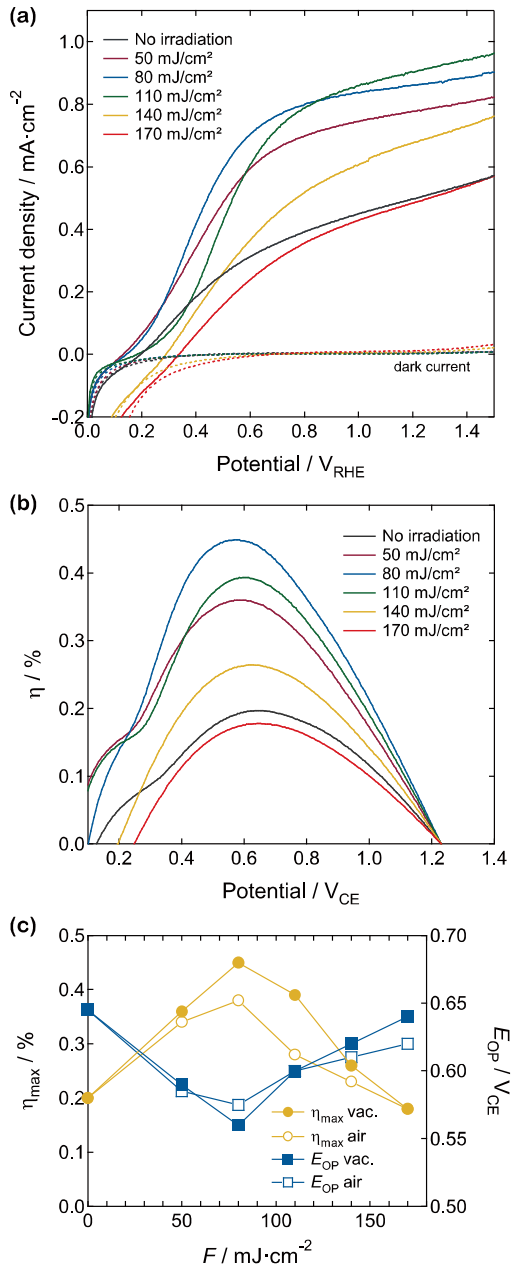

Fig. 10 (a) *J-V* curves and (b) η of pristine TiO_2 and TiO_{2-x} photoanodes laser irradiated under vacuum, measured under simulated solar light at 100 mW·cm^{-2} in 1 M KOH electrolyte (pH = 13.6). (c) η_{max} and E_{OP} for the TiO_{2-x} photoanodes irradiated under vacuum and in air as a function of laser fluence.

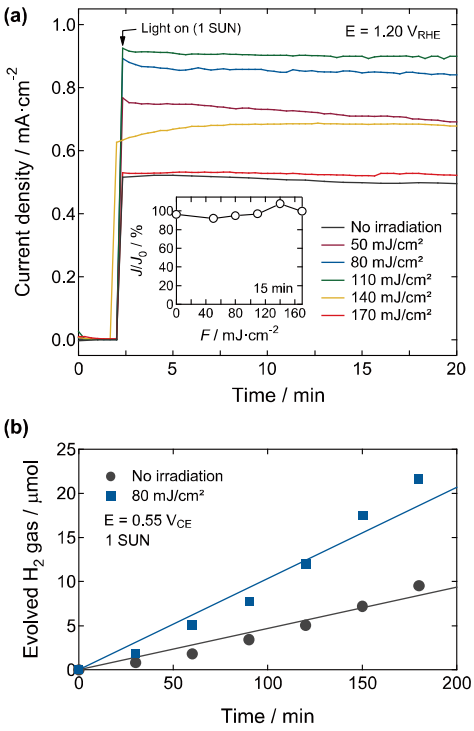

Fig. 11 Time dependences of (a) Photocurrent and (b) H_2 evolution of pristine TiO_2 and TiO_{2-x} photoanodes laser irradiated under vacuum, measured under simulated solar light at 100 mW·cm^{-2} in 1 M KOH electrolyte (pH = 13.6). The inset of (a) shows the ratio of photocurrent at 15 min from the starting excitation as a function of irradiated laser fluence.

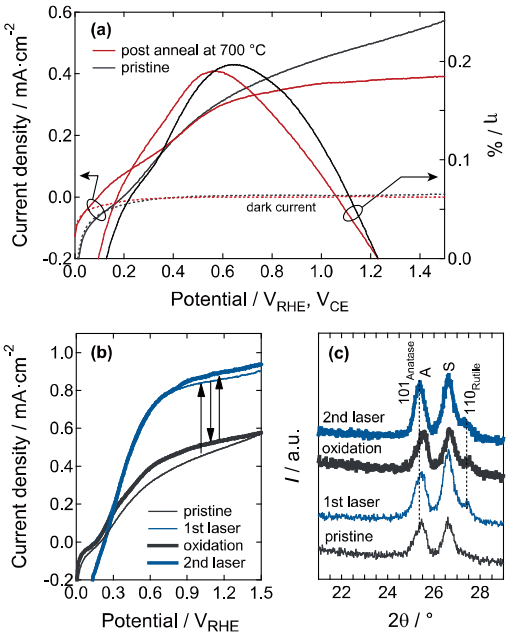

Fig. 12 (a) *J-V* curves and η of the pristine and post-annealed (700 °C) TiO_2 photoanodes under simulated solar light at 100 mW·cm^{-2} in 1 M KOH electrolyte (pH = 13.6). (b) The *J-V* curves of $TiO_{2-x}(TiO_2)$ photoanodes for first laser irradiation, oxidation, and second laser irradiation. (c) GIXRD spectra of the $TiO_{2-x}(TiO_2)$ photoanodes corresponding to (b). The subscripts A and S represent Al_2O_3 and SnO_2:Sb, respectively.

A concern generally arises for the origin of photocurrent in the oxygen deficient photoanodes whether the observed photocurrent is derived from the water splitting or a self-oxidation of photoanodes. However, the possibility of self-oxidation effect was eliminated in our samples by following results. Figure 11a shows photocurrent stability of pristine TiO_2 and oxygen deficient TiO_{2-x} photoanodes at 1.20 V_{RHE}. The photocurrent of pristine TiO_2 after 15 min from the starting excitation kept 96% from the initial value. The laser irradiated samples also showed comparably high stability of photocurrent: it kept 92–107% at 15 min, indicating the continuous PEC reaction. Moreover, we successfully observed a H_2 evolution from both samples with and without the laser irradiation under 100 mW·cm^{-2} excitation at 0.55 V_{CE}. The H_2 gas evolution rates for pristine and laser irradiated (80 mJ·cm^{-2}) samples were calculated as 8.4 and 18.7 μmol·h^{-1}·cm^{-2}, respectively. The enhancement of H_2 evolution rate in the laser irradiated sample almost corresponded with the increase of photocurrent. These results evidence that the laser irradiated TiO_{2-x} photoanode demonstrated the intrinsic water splitting and the enhancement of PEC property.

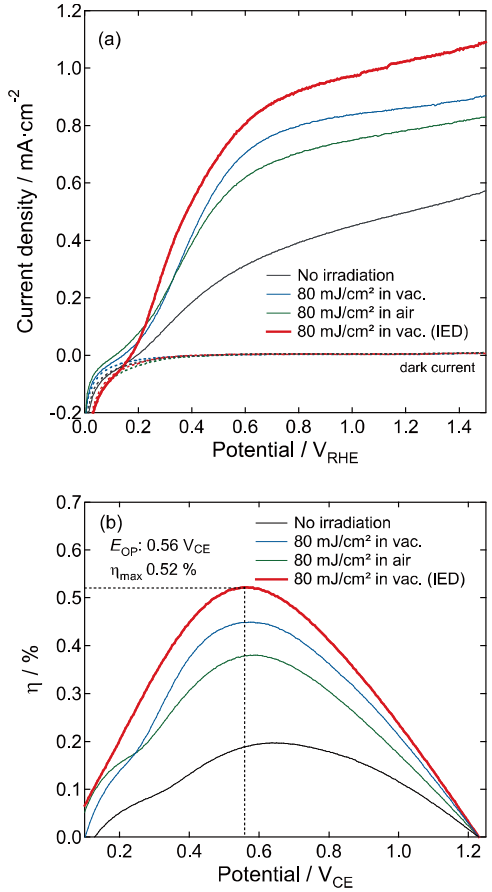

Fig. 13 (a) *J-V* curves and (b) η for the pristine TiO_2 and laser-irradiated TiO_{2-x} photoanodes under simulated solar light at 100 mW·cm^{-2} in 1 M KOH electrolyte (pH = 13.6). The laser irradiation was carried out at 80 mJ·cm^{-2} under vacuum (conventional and IED) and in air.

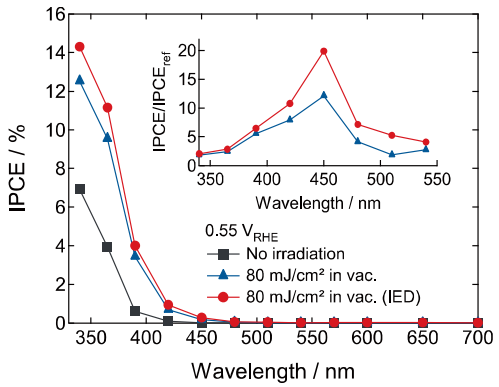

Fig. 14 IPCE spectra of the photoanodes as a function of the excitation wavelength at 0.55 V_{RHE}. The inset shows the IPCE ratio between the pristine TiO_2 and laser-irradiated TiO_{2-x} photoanodes.

Figure 12a shows the photocurrent density and η of the TiO_2 photoanode post-annealed at 700 °C. Post-annealing reduced E_{onset}, although it did not enhance the η value, indicating that the formation of the interface between the anatase and rutile phases did not increase the photocurrent in this system. In addition, we examined the continuous post treatment dependence of the photocurrent density of the TiO_{2-x}(TiO_2) photoanodes. Figure 10a shows that the laser irradiation at 80 mJ·cm^{-2} under vacuum produced a large increase in the photocurrent. This sample was post-annealed at 500 °C for 1 h, and the photocurrent of the sample was reduced to a value similar to that for the pristine TiO_2 photoanode (Fig. 12b). After post-annealing, the sample was irradiated again at 80 mJ·cm^{-2} under vacuum, and the photocurrent recovered to the original value for the TiO_{2-x} photoanode. During these treatments, the peak intensity of the GIXRD patterns and the rutile content were almost unchanged (Fig. 12c). This means that the enhancement of the PEC property in the laser-irradiated samples did not originate from the heterointerface, but arose from the oxygen deficiency of the TiO_2 films that improved the absorption of the excitatory light over a wide range of wavelengths.

Figure 13a shows the photocurrent density of the laser-irradiated TiO_{2-x} photoanode prepared by IED with an optimum fluence at 80 mJ·cm^{-2} under vacuum. The E_{onset} was reduced to 0.175 V_{RHE}, and the photocurrent at 1.23 V_{RHE} reached 1.029 mA·cm^{-2}. η_{max} was 0.52% at 0.560 V_{RHE} (Fig. 13b). This high η_{max} was 2.6-fold higher than that of the pristine TiO_2 photoanode, and was probably caused by the increase in the surface area by IED.

Figure 14 shows the IPCE spectra of pristine TiO_2 and laser-irradiated (80 mJ·cm^{-2} under vacuum) TiO_{2-x} photoanodes at 0.55 V_{RHE}. The IPCE of the TiO_2 photoanode was 6.9% at 340 nm, and decreased to almost zero at around 400 nm. However, in the laser-irradiated TiO_{2-x} photoanodes, the photoresponse was maintained at 480 nm because of the large absorbance of visible light wavelengths (Fig. 4), and the IPCE in the UV range also increased to 12.5% at 340 nm. The IPCE reached 14.3% in the TiO_{2-x} photoanode prepared by IED, and its visible

range response was 20-fold greater than that of the pristine TiO_2 photoanode at 450 nm.

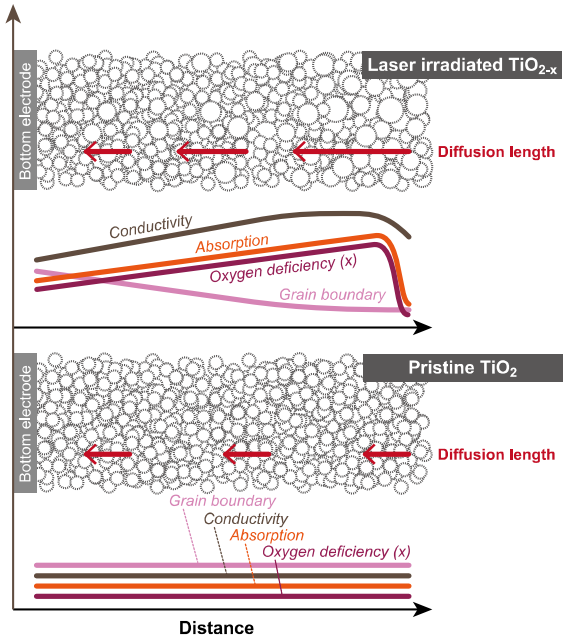

Fig. 15 Schematic illustrations of the structural and physical properties of the pristine TiO_2 and laser-irradiated TiO_{2-x} photoanodes.

The main origin of PEC property enhancement in the oxygen deficient TiO_{2-x} photoanodes would be the high IPCE in the UV wavelength range. The oxygen vacancy in TiO_2 can increase the electron donor density, resulting in the improvement of charge transport and the shifting Fermi level of TiO_2 toward the conduction band.[35–37] This would lead to stimulate the charge separation at the reaction interface, which is linked to the enhancement of water splitting. Moreover, the characteristic cross-sectional morphology in the laser irradiated samples would also contribute the enhancement of PEC property. The structural and physical properties of the pristine and laser-irradiated photoanodes are summarized in Fig. 15. The crystallite size and stoichiometric oxygen content are uniform in the pristine TiO_2 layer; therefore, the number of grain boundaries, conductivity, and reduced absorbance for visible light are also homogeneous. In contrast, the laser-irradiated samples would have a gradient distribution of crystallite sizes and oxygen deficiency; the crystallite size and oxygen deficiency increased toward the top surface, although the oxygen deficiency at the top surface was eliminated by reoxidation. The crystallite growth reduced the number of grain boundaries, and the oxygen deficiency enhanced the bulk conductivity. Both of them would increase the majority carrier diffusion length, which is crucial for improving the PEC activity.[38,39] Furthermore, because visible light penetrate deeper into the photoanode than UV light, the improved absorption in the visible range means that the interior of the photoanode is used more efficiently. The extended diffusion length of the excited carriers and efficient use of the excitatory light improve the solar water splitting properties of the laser-irradiated photoanodes.

Thus, we have shown that blackening titania photoanodes by the laser irradiation resulted in a high PEC property for solar water splitting. Moreover, the application of this technique to nanostructured TiO_2 is expected to produce further high-performance photoanodes.

Conclusions

We have demonstrated that pulsed UV laser irradiation of TiO_2 films is a simple, effective process for making oxygen-deficient black titania (TiO_{2-x}) films. The oxygen-deficient TiO_{2-x} photoanodes were fabricated by KrF laser irradiation under low-vacuum conditions for several minutes. The resulting TiO_{2-x} film had a larger absorbance for visible light than pristine TiO_2, and it showed a higher PEC property for solar water splitting. The STH efficiency of the TiO_{2-x} photoanode was 0.52%, which was 2.6-fold higher than that of the pristine TiO_2 photoanode. Our rapid fabrication process for black titania photoanodes has great potential for industrial solar hydrogen production.

Notes and references

[a] *Advanced Manufacturing Research Institute, National Institute of Advanced Industrial Science and Technology, Tsukuba Central 5, 1-1-1 Higashi, Tsukuba, Ibaraki 305-8565, Japan. Tel: +81-29-861-6368; E-mail: t-nakajima@aist.go.jp*

† Electronic Supplementary Information (ESI) available: [details of any supplementary information available should be included here]. See DOI: 10.1039/b000000x/

1 B. D. Alexander, P. J. Kulesza, I. Rutkowska, R. Solarska and J. Augustynski, *J. Mater. Chem.*, 2008, **18**, 2298.
2 J. Nowotny, T. Bak, M. K. Nowotny and L. R. Sheppard, *Int. J. Hydrog. Energy*, 2007, **32**, 2609.
3 C. X. Kronawitter, L. Vayssieres, S. Shen, L. Guo, D. A. Wheeler, J. Z. Zhang, B. R. Antoun and S. S. Mao, *Energy Environ. Sci.*, 2011, **4**, 3889.
4 F. E. Osterloh, *Chem. Soc. Rev.*, 2013, **42**, 2294.
5 Y. Park, K. J. McDonald and K-S. Choi, *Chem. Soc. Rev.*, 2013, **42**, 2321.
6 T. Hisatomi, F. L. Formal, M. Cornuz, J. Brillet, N. Tétreault, K. Sivula and M. Grätzel, *Energy Environ. Sci.*, 2011, **4**, 2512.
7 X. Liu, F. Wang and Q. Wang, *Phys. Chem. Chem. Phys.*, 2012, **14**, 7894.
8 R. Saito, Y. Miseki and K. Sayama, *Chem. Commun.*, 2012, **48**, 3833.
9 B. A. Pinaud, P. C. K. Vesborg and T. F. Jaramillo, *J. Phys. Chem. C*, 2012, **116**, 15918.
10 M. Grätzel, *Nature*, 2001, **414**, 338.
11 A. Fujishima, X. Zhang and D. A. Tryk, *Surf. Sci. Rep.*, 2008, **63**, 515.
12 M. R. Hoffmann, S. T. Martin, W. Choi and D. W. Bahnemann, *Chem. Rev.*, 1995, **95**, 69.
13 X. Chen, L. Liu, P. Y. Yu and S. S. Mao, *Science*, 2011, **331**, 746.
14 T. Leshuk, R. Parviz, P. Everett, H. Krishnakumar, R. A. Varin and F. Gu, *ACS Appl. Mater. Interfaces*, 2013, **5**, 1892.
15 C. Yang, Z. Wang, T. Lin, H. Yin, X. Lü, D. Wan, T. Xu, C. Zheng, J. Lin, F. Huang, X. Xie and M. Jiang, *J. Am. Chem. Soc.*, 2013, **135**, 17831.
16 Z. Wang, C. Yang, T. Lin, H. Yin, P. Chen, D. Wan, F. Xu, F. Huang, J. Lin, X. Xie and M. Jiang, *Energy Environ. Sci.*, 2013, **6**, 3007.
17 M. M. Khan, S. A. Ansari, D. Pradhan, M. O. Ansari, D. H. Han, J. Lee and M. H. Cho, *J. Mater. Chem. A*, 2014, **2**, 637.

18 T. Nakajima, K. Shinoda and T. Tsuchiya, *Chem. Soc. Rev.*, 2014, DOI: 10.1039/c3cs60222b.
19 T. Nakajima, T. Tsuchiya, M. Ichihara, H. Nagai and T. Kumagai, *Chem. Mater.*, 2008, **20**, 7344.
20 T. Nakajima, T. Tsuchiya, M. Ichihara, H. Nagai and T. Kumagai, *Appl. Phys. Express*, 2009, **2**, 023001.
21 T. Tsuchiya, A. Watanabe, Y. Imai, H. Niino, I. Yamaguchi, T. Manabe, T. Kumagai and S. Mizuta, *Jpn. J. Appl. Phys.*, 1999, **38**, L823.
22 T. Nakajima, K. Shinoda and T. Tsuchiya, *Phys. Chem. Chem. Phys.*, 2013, **15**, 14384.
23 Y. F. Joya and Z. Liu, *Scr. Mater.*, 2009, **60**, 467.
24 T. Nakajima, T. Tsuchiya and T. Kumagai, *J. Solid State Chem.*, 2009, **182**, 2560.
25 Y. L. Page and P. Strobel, *J. Solid State Chem.*, 1983, **47**, 6.
26 W-Q. Han and Y. Zhang, *Appl. Phys. Lett.*, 2008, **92**, 203117.
27 Bäuerle, D.: *Laser Processing and Chemistry* (Springer-Verlag Berlin Heidelberg New York 2000)
28 T. Nakajima, T. Kitamura and T. Tsuchiya, *Appl. Catal. B-Environ.*, 2011, **108-109**, 47.
29 S. Kačiulis, G. Mattogno, A. Napoli, E. Bemporad, F. Ferrari, A. Montenero and G. Gnappi, *J. Electron Spectrosc. Relat. Phenom.*, 1998, **95**, 61.
30 G. Wang, H. Wang, Y. Ling, Y. Tang, X. Yang, R. C. Fitzmorris, C. Wang, J. Z. Zhang and Y. Li, *Nano Lett.*, 2011, **11**, 3026.
31 G. Liu, H. G. Yang, X. Wang, L. Cheng, H. Lu, L. Wang, G. Q. Lu and H-M. Cheng, *J. Phys. Chem. C*, 2009, **113**, 21784.
32 X. Pan, M-Q. Yang, X. Fu, N. Zhang and Y-J. Xu, *Nanoscale*, 2013, **5**, 3601.
33 K. T. Jacob and S. Gupta, *JOM*, 2009, **61**, 56.
34 B. Prasai, B. Cai, M. K. Underwood, J. P. Lewis and D. A. Drabold, *J. Mater. Sci.*, 2012, **47**, 7515.
35 D. C. Cronemeyer, *Phys. Rev.*, 1959, **113**, 1222.
36 A. Janotti, J. B. Varley, P. Rinke, N. Umezawa, G. Kresse and C. G. Van de Walle, *Phys. Rev. B*, 2010, **81**, 085212.
37 Y. H. Hu, *Angew. Chem. Int. Ed.*, 2012, **51**, 12410.
38 S. Södergren, A. Hagfeldt, J. Olsson and S-E. Lindquist, *J. Phys. Chem.*, 1994, **98**, 5552.
39 W. H. Leng, P. R. F. Barnes, M. Juozapavicius, B. C. O'Regan and J. R. Durrant, *J. Phys. Chem. Lett.*, 2010, **1**, 967.

